Radio-isotopes in Fusion–Fission Hybrid Reactors*

Marcus Turner-Wood†
Department of Physics, University of Liverpool
(Dated: October 15, 2025)

This report explores activation and shielding studies supporting hybrid (fusion–fission) blanket design. Gold foils irradiated in water and carbon moderators gave a thermal-flux ratio $R = \phi_{\mathrm{th}}^{(\mathrm{water})}/\phi_{\mathrm{th}}^{(\mathrm{carbon})} = 4.95\pm1.13$, indicating higher inferred thermal flux in water for the tested geometry. Vanadium activation yielded a fitted half-life $T_{1/2}(^{52}\mathrm{V}) = 190.2\pm1.5$ s (3.169 ± 0.025 min), 15.3% below the NuDat3 reference, with plausible systematics discussed. Detector full-energy-peak efficiencies were modelled with LabSOCS and validated independently using a six-peak europium source with decay correction from 01/10/2014 and the recommended $T_{1/2}(^{152}\mathrm{Eu}) = 13.517$ y ($\approx 4\,937$ d). A bench β-attenuation test in aluminium supports a layered shield concept (low-Z / hydrogenous / borated / high-Z / concrete). Results inform moderator placement, TBR margins, shielding, and maintenance windows in hybrids.

I. INTRODUCTION

The global demand for reliable, low-carbon energy is more pressing than ever. While renewable sources such as solar and wind have been developed to an incredible standard, their intermittency demands secure and independent energy supply. Nuclear fission has provided such baseload energy but recent advances in plasma physics, materials science, and engineering have pushed magnetic and inertial confinement fusion closer to viability. Fusion promises vast quantities of clean energy with minimal long-lived waste.

This report examines concepts and design considerations for *fusion–fission hybrid* reactors, which combine a 14.1 MeV D–T fusion neutron source with a subcritical fission blanket. This paper reviews source-driven multiplication and blanket missions; the role of moderators versus multipliers in first-wall and blanket design; activation of material with emphasis on ^{52}V half-life implications for maintenance and waste; activation foils (In, Au) and absolute detector efficiency with simulation (LabSOCS) as well as shielding strategies for the mixed neutron–gamma fields characteristic of hybrids. The measured environmental background spectrum referred to throughout is shown in Fig. 1.

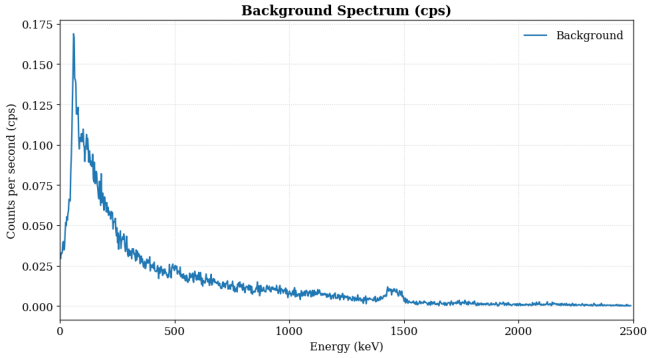

FIG. 1. Background spectrum (counts per second) versus energy measured with a NaI(Tl) scintillation crystal. Axes carry units; markers show data points.

II. BASICS OF A FUSION–FISSION HYBRID REACTOR

Fusion–fission hybrids couple a 14.1 MeV D–T neutron source to a subcritical blanket ($k_{\mathrm{eff}} < 1$) to multiply source neutrons, breed fuel, and transmute actinides while retaining the safety margin of subcriticality. The source-driven neutron multiplication can be approximated by

$$M_n \approx \frac{1}{1 - k_{\mathrm{eff}}}, \tag{1}$$

so neutron flux and blanket power scale roughly as $S\,M_n$, where S is the external source strength. Designs often target $k_{\mathrm{eff}} \lesssim 0.95$ for margin; some concepts pursue deeper subcritical operation (e.g., $k_{\mathrm{eff}} < 0.7$) for additional safety [3, 4]. With China announcing plans to operate the world's first hybrid fusion–fission plant by 2030 [2], the hybrid reactor is timely and relevant, and Velikhov—often called the "Godfather of ITER"—hailed hybrids as "key to the nuclear renaissance" [1].

The blanket composition and the neutron spectrum are chosen to optimise performance, sustainability, and radiation controls. Energy production and U–Pu breeding rely on sustained $^{238}\mathrm{U}(n,\gamma)\rightarrow{}^{239}\mathrm{Pu}$ with subsequent fission, while Th–U breeding proceeds via $^{232}\mathrm{Th}(n,\gamma)\rightarrow{}^{233}\mathrm{U}$. Spectrum tailoring seeks the desired capture paths without sacrificing reactivity or power density; waste transmutation targets both fission and capture in higher actinides to reduce radiotoxicity and decay heat. Tritium self-sufficiency requires TBR > 1, fast-spectrum fission power must be delivered at acceptable damage

* Draft formatted in REVTEX 4.2 style.
† sgmturn2@liverpool.ac.uk

rates to structures, and inventories of long-lived products are limited by activation controls and impurity management. In practice, liquid fluoride salts such as FLiBe (Li_2BeF_4) or FLiNaBe provide tritium via $^6Li(n,\alpha)t$ and furnish mild moderation; ^{6}Li enrichment, redox control, and salt temperature set breeding performance, corrosion behaviour, and tritium extraction efficiency. Neutron multipliers are introduced to meet TBR and sustain the fast tail: beryllium is especially effective because $^9Be(n,2n)$ enhances the fast population and improves neutron economy [5, 6]; lead offers complementary properties—its $(n,2n)$ is thresholded, but Pb provides thermal inertia and aids shielding [7]. For plasma-facing components, tungsten tiles remain favoured for erosion resistance and high-temperature strength, while Be first walls (as in ITER) add $(n,2n)$ but require stricter handling and dust-safety protocols [8, 9]. Overall, hybrids benefit from a predominantly fast spectrum near the first wall to sustain fission of higher actinides and to meet TBR, with limited, well-placed moderation introduced deeper in the blanket to steer capture paths without undermining fast-spectrum objectives. The activation measurements reported later (Sections III and V) provide ground truth for transport models that set k_{eff} margins, shield thicknesses, and maintenance windows.

III. MODERATORS AND THE FIRST WALL

Introduction

Moderation is applied carefully so as not to compromise subcriticality and fast-spectrum functions. For actinide burning and waste transmutation, a predominantly fast spectrum means efficient fission of higher actinides and decreases parasitic capture. In contrast, specific features of the Th cycle and local power shaping needs may benefit from spectrum softening. In practice, moderation is introduced deeper within the blanket, whereas the near-wall region prioritises multipliers and structural resilience.

Experiment / Methods

Energy calibration (Na-22). Prior to any measurements a sealed ^{22}Na source was used to calibrate the NaI(Tl)+PMT energy scale at the same source–detector geometry as used for the foil measurements. Spectra were acquired and Gaussian peaks were fitted to the lines at 511 keV and 1274.5 keV. The calibration was applied in ProSpect [33], which was the software used to acquire and analyse the spectra in this section.

Background measurement. A background γ spectrum was acquired with a NaI(Tl) scintillation crystal coupled to a PMT and positioned behind lead shielding (see Appendix B for detector details in the course handout; not reproduced here). The electronics were warmed up for ∼15 min to stabilise high-voltage gain, after which a background spectrum was acquired for $(4.229 \pm 0.001) \times 10^3$ s and saved (see Fig. 1).

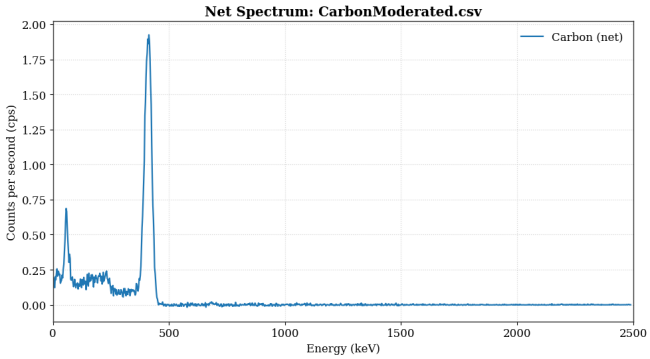

FIG. 2. Net NaI(Tl) spectrum for the **water-moderated** ^{198}Au foil; dashed lines indicate expected γ energies from NuDat3 markers (411.8, 675.9, 1087.7 keV) [27].

Au-foil moderation comparison. A thin gold foil was placed within the centre of a moderator block (water and graphite) and irradiated with an (^{241}Am–^{9}Be) neutron source for two fixed durations: (691200 ± 60) s and (9849600 ± 60) s, respectively. After irradiation, the foil was transferred with a delay of about 60 ± 15 s to the NaI(Tl)+PMT detection setup, positioned within the lead shielding at a fixed source–detector distance, and a spectrum was acquired for the live times 436.67 ± 0.01 s (water) and 381.66 ± 0.01 s (carbon). The sequence was repeated with the alternative moderator. Acquisition settings and geometry were held as constant as reasonably possible. Gaussian curves were fitted over the peaks. **No per-peak ROI window counting was used here: the background was taken from the separately acquired spectrum and live-time scaled for subtraction.**

Results

Background spectrum. The background spectrum (Fig. 1) was characteristic of lab radiation. A distinct feature near ∼1461 keV was observed and is consistent with the ^{40}K line at 1460.8 keV.

Relative flux results (rounded).

$$R \equiv \frac{\phi_{\text{th}}^{(\text{water})}}{\phi_{\text{th}}^{(\text{carbon})}} = 4.95 \pm 1.13.$$

Au moderation comparison. The **water-moderated** configuration yielded a larger net 411.8 keV peak area than the carbon-moderated configuration, implying a higher inferred thermal flux in **water** ($R > 1$). Peak-to-marker energy residuals were small (few keV), consistent with NaI(Tl) resolution and minor gain drift. Table I summarises the marker comparison with Fig. 2 showing the spectrum (water-moderated).

TABLE I. Peak vs. marker for Au-foil runs (rounded to NaI resolution; energies in keV; rates in cps).

File	Isotope	Expected (keV)	Found (keV)	ΔE (keV)	Peak (cps)
WaterModerated	^{198}Au	411.8	413.8	2.0	1.925
WaterModerated	^{198}Au	675.9	687.1	11.2	0.0216
WaterModerated	^{198}Au	1087.7	1094.6	6.9	0.0127
CarbonModerated	^{198}Au	411.8	408.2	-3.6	0.3617
CarbonModerated	^{198}Au	675.9	677.3	1.5	0.0164
CarbonModerated	^{198}Au	1087.7	1084.0	-3.7	0.0085

Interpretation

Hydrogenous moderators (water) have a large average logarithmic energy decrement per collision ($\xi \approx 1$ for hydrogen), therefore they thermalise fast neutrons efficiently. Graphite (carbon), by contrast, moderates more slowly ($\xi \approx 0.16$) [32] but has very low absorption compared to water, preserving epithermal/fast tails (valuable in fast or breeder reactors). In compact moderators, faster thermalisation in water means it is the better option at larger thicknesses, but absorption from hydrogen can offset these benefits depending on the mission. Because the water and carbon runs shared the same geometry and settings, many systematics cancel in the ratio R. **The 2.223 MeV H-capture line was negligible here**, but it is a consideration in hydrogenous designs.

IV. FIRST-WALL MATERIALS VERSUS MODERATORS

Discussion

Choosing the plasma-facing materials depends mainly on material durability under high heat flux, optimising the tritium breeding ratio (TBR) as well as the neutron spectrum that the blanket receives. Tungsten remains the default choice because it tolerates extreme heat fluxes and erosion while keeping microscopic stability under irradiation [8, 9]. Beryllium, when used as plasma-facing or near-wall material, adds neutron multiplication via $^{9}\mathrm{Be}(n, 2n)$ but brings handling, dust, and end-of-life issues that must be designed in from the start [26]. Moderators are deliberately kept away from the first wall. Placing graphite, water, or moderating polymers at depth allows spectrum control under lower thermal and radiation loads, and therefore avoids compromising the TBR at the surface. In liquid blankets, the carrier (e.g. a fluoride or lithium–lead) already provides mild moderation and tritium breeding. Be or Pb inserts are then tuned to increase multiplication and regulate the TBR, while maintaining thermal durability and strength [5–7].

V. V–52 HALF–LIFE: MAINTENANCE AND WASTE

Introduction

Vanadium alloys (e.g. V-4Cr-4Ti) are attractive low-activation materials for first walls and blankets due to their favourable activated products and high-temperature endurance [10–12]. Under irradiation, natural ^{51}V (99.75%) captures a neutron to form ^{52}V, which decays by β^- to ^{52}Cr with $t_{1/2} = 3.743$ min [13, 14]:

$$^{51}\mathrm{V}(n,\gamma)^{52}\mathrm{V} \xrightarrow[t_{1/2}=3.743\ \mathrm{min}]{\beta^-} {}^{52}\mathrm{Cr} + \gamma. \qquad (2)$$

Theoretical formulation

Counts vs. time were modelled as

$$y(t) = B + Ae^{-kt}, \qquad k = \frac{\ln 2}{T_{1/2}}, \qquad (3)$$

with B fixed from an early baseline window and the decay fit applied after detector transients subsided.

Experiment

A vanadium sample was irradiated near a ^{241}Am–Be neutron source for a fixed time and transferred over a short, timed interval to a NaI(Tl) detector behind lead at a fixed source–detector distance. Counts with a dwell of 1.00 ± 0.01 s were acquired over $\sim$2050 s; a graph of count rate against time was fitted to the model above with B estimated from $t \leq 400$ s and the fit applied for $t \geq 560$ s.

Results

Using the model above, the fitted parameters are

$$B = 14.705 \pm 0.2 \text{ cps},$$
$$A = 1250.92 \pm 28 \text{ cps},$$
$$k = (3.64522 \pm 0.000028) \times 10^{-3} \text{ s}^{-1},$$
$$T_{1/2} = 190.2 \pm 1.5 \text{ s}.$$

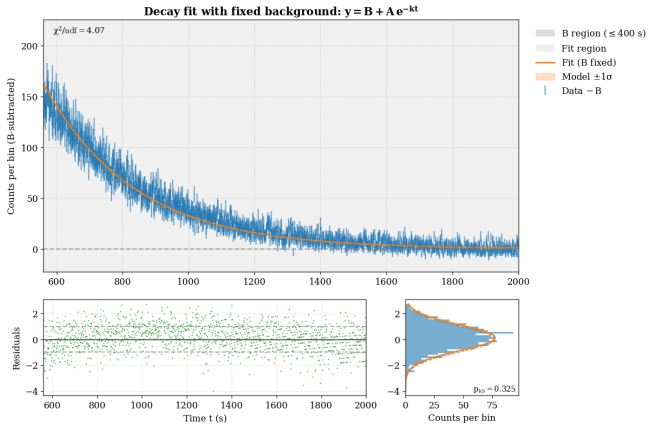

FIG. 3. Decay fit for ^{52}V with fixed background (top) and residual analysis (bottom). Points show rates with Poisson error bars; the line shows the best fit.

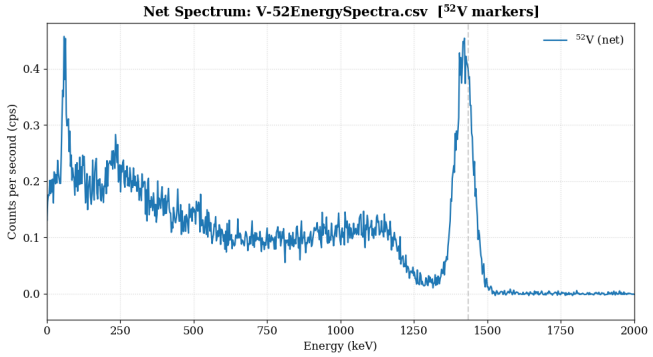

FIG. 4. NaI(Tl) energy spectrum (cps) for ^{52}V with level-energy markers. Axes are labelled with units; markers show data and counting uncertainty.

Goodness-of-fit: $\chi^2/\mathrm{ndf} = 4.074$. The fitted half-life is 3.169 min, which is 15.3% lower than the NuDat3 reference (3.743 min).

Energy Spectra

Energy spectra of ^{52}V were recorded to check for impurities or secondary emitters. In addition to the principal peak near 1490 keV, a low-energy continuum was observed on its left-hand side. This feature is consistent with Compton scattering of γ rays in the detector and surrounding materials as well as bremsstrahlung generated in the lead shielding. These processes cause the continuum below the full-energy peak and do not, by themselves, imply the presence of additional nuclides.

Interpretation

Even with the underestimate, the steep decay demonstrates rapid short-term dose reduction: $A(t) = A_0\, 2^{-t/t_{1/2}}$ implies that after 15 min (≈ 4.7 half-lives by the fit), activity is ($\sim A_0/26$); after 30 min, ($\sim A_0/7.1 \times 10^2$); after one hour, ($\sim A_0/5 \times 10^5$). Potential error sources include ROI selection, gain drift, and the accuracy of the background estimate, any of which can inflate χ^2/ndf. **Waste classification and materials control:** because ^{52}V decays rapidly, V-alloy components tend to "decay out" with respect to other short-lived sources. **Measurement planning:** post-shutdown spectroscopy will feature ^{52}V as a radiation indicator. Count plans should include changing rates and decay corrections. Detector placement, shielding choices, and times are best chosen with simulated growth and decay curves to maximise worker protection.

VI. INDIUM, DETECTOR EFFICIENCY, AND SIMULATION

Introduction

Indium is a classic activation monitor: natural ^{115}In captures a neutron to form $^{116\mathrm{m}}$In ($t_{1/2} \approx 54.2$ min), emitting strong γ-rays suitable for HPGe semiconductor counting. Cadmium covers are commonly used to separate thermal from epithermal neutrons. Inelastic production of $^{115\mathrm{m}}$In ($t_{1/2} \approx 4.5$ h) may also appear [20, 28].

Theoretical formulation

Absolute photopeak efficiency at energy E enters the activity relation

$$A_c(E) = \frac{N_{\mathrm{net}}}{t_\ell\, \varepsilon(E)\, I_\gamma}, \tag{4}$$

where A_c is activity at count start, N_{net} the net peak area, t_ℓ the live time, $\varepsilon(E)$ the full-energy-peak efficiency, and I_γ the absolute emission probability. Activities are corrected to removal via

$$A_{\mathrm{rem}} = A_c\, \mathrm{e}^{\lambda \Delta t}, \qquad \lambda = \frac{\ln 2}{T_{1/2}}, \tag{5}$$

and, when inferring flux during irradiation of time t_{irr}, the build-up factor

$$B_{\mathrm{irr}} = \frac{1}{1 - \mathrm{e}^{-\lambda t_{\mathrm{irr}}}} \tag{6}$$

is applied.

Experiment / Methods

Computational Monte Carlo (LabSOCS) modelling was used to obtain an energy-dependent full-energy-peak efficiency curve $\varepsilon(E)$ for the specific detector and geometry, based on the manufacturer's crystal characterisation and a 3D model including source–detector distance, sample size, matrix composition/density, and Pb shielding [21–24]. Self-attenuation and external attenuation were included; coincidence summing and angular effects were evaluated within LabSOCS.

To validate $\varepsilon(E)$, a certified Eu calibration source with peaks at (122, 245, 344, 779, 964, 1408 keV) was measured in the identical geometry. The certificate activity at the reference date $t_0 = 01/10/2014$ was $A_{\mathrm{ref}} = 0.0035$; decay to the measurement date t used $T_{1/2}(^{152}\mathrm{Eu}) = 13.517$ y ($\approx 4\,937$ days):

$$A_{\mathrm{Eu}}(t) \;=\; A_{\mathrm{ref}}\, 2^{-\frac{t-t_0}{T_{1/2}}}.$$

Absolute efficiencies at the Eu lines were then obtained from

$$\varepsilon(E_i) = \frac{N_{\mathrm{net},i}}{t_\ell\, A_{\mathrm{Eu}}(t)\, I_{\gamma,i}}.$$

Activation samples were irradiated for fixed t_{irr}, transferred with delay $\Delta t = 60 \pm 15$ s, and counted for live time t_ℓ. Net peak areas came from Gaussian fits with linear sidebands.

Results

Eu comparison and fit. At the time of measurement, the Eu activity was $A_{\mathrm{Eu}} = 9.829 \times 10^4$ Bq, and the Eu spectrum live time was $t_\ell = 506.32 \pm 0.01$ s. Absolute full-energy-peak efficiencies were fitted with a weighted quadratic in $\log_{10} E$ [29–31]:

$$\begin{aligned} \log_{10}\varepsilon(E) &= a_0 + a_1 \log_{10} E + a_2 \big(\log_{10} E\big)^2, \\ \{a_0, a_1, a_2\} &= \{-2.926781,\ 0.117701,\ -0.214223\}. \end{aligned} \tag{7}$$

Figure 5 compares the LabSOCS points (and their fit) with the Eu data (and the Eu-based fit). A goodness-of-fit of $\chi^2/\mathrm{ndf} = 3.07$ for the Eu dataset was obtained. Residuals versus energy with 1σ error bars are shown in Fig. 6.

Indium spectrum checks. Peak energies from the $^{116\mathrm{m}}$In spectrum are consistent with NuDat3 markers within the NaI(Tl) setup's resolution. Centroids were then compared to expectation; see Table II.

Per-peak activities and combined result. For the four principal $^{116\mathrm{m}}$In lines, activities at removal were calculated using the validated $\varepsilon(E)$ and a decay back-correction to the count start (Table III). The inverse-variance–weighted average is

$$A_{\mathrm{rem}}\big(^{116\mathrm{m}}\mathrm{In}\big) = (1.280 \pm 0.125) \times 10^4 \text{ Bq}.$$

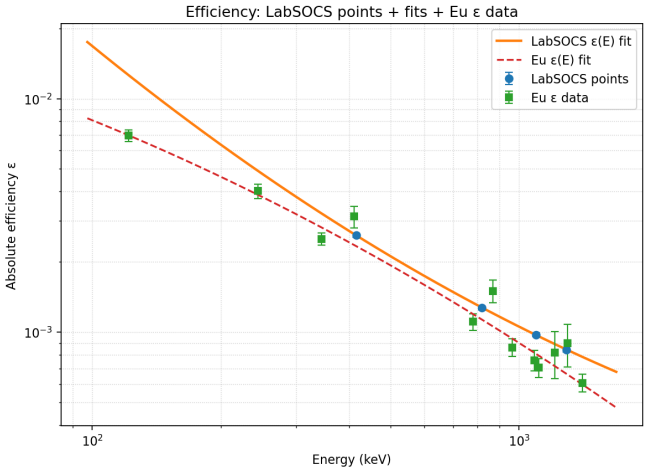

FIG. 5. Absolute efficiency validation: LabSOCS points and fit; Eu data overlaid with the Eu-based fit.

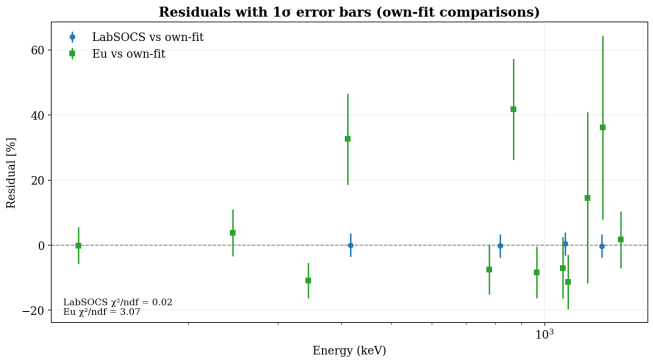

FIG. 6. Residuals (percent) of LabSOCS and Eu datasets with respect to their fits (with 1σ error bars).

Thermal flux from indium. Using the activation build-up and decay model with the validated $\varepsilon(E)$, the thermal neutron flux inferred from the indium foil is

$$\Phi = (1.978 \pm 0.218) \times 10^4 \text{ n cm}^{-2}\,\text{s}^{-1}.$$

Interpretation

Because the LabSOCS setup and the Eu/In measurements were independent, this constitutes a validation of the LabSOCS model rather than a circular calibration. A distributed set of foils (In, Au, Ni) across the blanket provides spectral and flux constraints to validate transport, improving confidence in k_{eff}, TBR, and transmutation rate predictions.

TABLE II. ^{116}In: expected vs. measured energies and peak rates.

Expected (keV)	Measured (keV)	ΔE (keV)	Peak (cps)
416.0	417.027439	+1.027439	0.079990
818.0	818.626077	+0.626077	0.013454
1097.0	1097.406265	+0.406265	0.039046
1293.0	1293.810081	+0.810081	0.044891

VII. SHIELDING OF RADIATION

Introduction

Hybrid systems produce a mixed radiation field of 14.1 MeV fusion neutrons, a spectrum of neutrons produced by fission as well as capture γ rays from structures, coolant, and activated products. Radiation shields must therefore address fast-neutron slowing, thermal-neutron capture, photon attenuation, and streaming/skyshine through penetrations while also remaining compact and maintainable. A simple test with a β source in aluminium provides an argument for the "low-Z first, high-Z later" design logic used in full mixed-field shielding.

Theoretical formulation

Net count rate after subtracting background is

$$r = \frac{C}{t_\ell} - \frac{B}{t_b}, \qquad u(r) = \sqrt{\frac{C}{t_\ell^2} + \frac{B}{t_b^2}}. \tag{8}$$

Assuming exponential attenuation in areal density ρx,

$$\ln r \;=\; m\,(\rho x) + c, \tag{9}$$

the half-thickness and a practical range are

$$d_{1/2} = \frac{\ln 2}{|m|\,\rho}, \qquad R_\beta \simeq 10\, d_{1/2}. \tag{10}$$

Experiment

A sealed ^{90}Sr source, an aluminium foil stack, and a GM tube were used to characterise electron attenuation in aluminium. For each total thickness x (mm), gross counts C were recorded over t_ℓ, and background counts B over t_b. Figures 7–8 show the data and the fitted exponential segment.

Results

The linear window contains 6 points with a reduced $\chi^2 = 4.93$. From Eq. (10) we obtain

$$d_{1/2} = (0.412 \pm 0.024)\ \text{mm}, \tag{11}$$

$$R_\beta \simeq (4.122 \pm 0.238)\ \text{mm} = (1.113 \pm 0.064)\ \text{g cm}^{-2}. \tag{12}$$

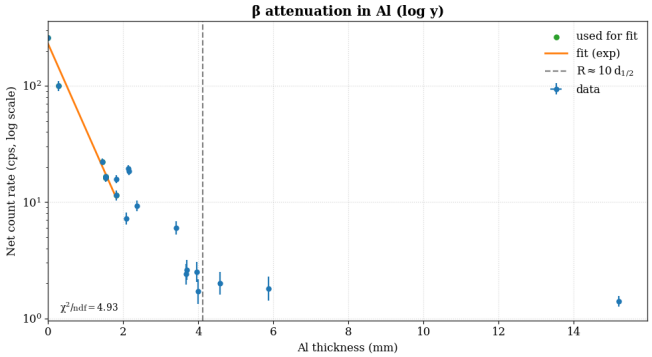

FIG. 7. β attenuation in Al: net rate vs thickness. The curve is the exponential implied by the linear fit in $\ln r$ vs areal density over the early window. The vertical dashed line marks $R_\beta \simeq 10\, d_{1/2}$.

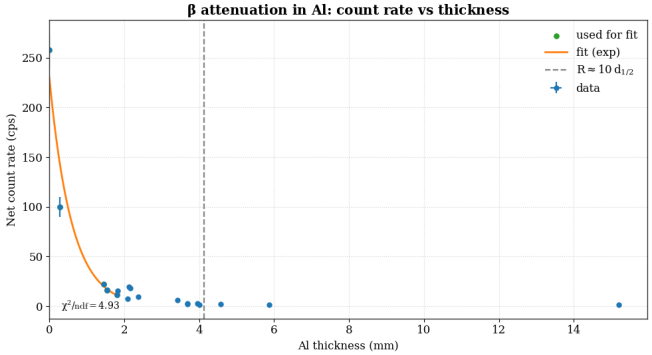

FIG. 8. Same data on a semilog axis. The straight segment in $\ln r$ vs thickness underpins the estimate of $d_{1/2}$ and R_β.

To convert the aluminium range to an endpoint energy, two-point interpolation was used on the Al CSDA range curve (ESTAR).[34] With ESTAR points $(R_1, E_1) = (1.040\ \text{g cm}^{-2}, 2.00\ \text{MeV})$ and $(R_2, E_2) = (1.230\ \text{g cm}^{-2}, 2.28\ \text{MeV})$,

$$E(R) = E_1 + \frac{E_2 - E_1}{R_2 - R_1}\,(R - R_1), \qquad \sigma_E \simeq \left|\frac{E_2 - E_1}{R_2 - R_1}\right| \sigma_R,$$

giving

$$E_{\max}^{(\text{ESTAR, 2-pt})} = (2.107 \pm 0.095)\ \text{MeV}.$$

As a check, inverting the Katz–Penfold aluminium range relation,

$$R_{\text{KP}}\ [\text{mg cm}^{-2}] \approx 412\, E^{1.265} - 95.4, \tag{13}$$

$$E(R_{\text{KP}}) = \left(\frac{R_{\text{KP}} + 95.4}{412}\right)^{1/1.265}, \tag{14}$$

yields

$$E_{\max}^{(\text{Katz–Penfold})} = (2.341 \pm 0.098)\ \text{MeV},$$

and hence the difference

$$\Delta \equiv E_{\text{KP}} - E_{\text{ESTAR, 2-pt}} = +0.234\ \text{MeV}.$$

TABLE III. ^{116m}In peaks and derived activities at removal.

Energy (keV)	p_γ	Gross counts	Live time (s)	$A_{\rm rem}$ (Bq)	$\sigma_{A_{\rm rem}}$ (Bq)
416.86	0.272	533	1677.06	2.0669×10^4	3.5512×10^3
818.72	0.366	140	1677.06	8.2941×10^3	1.5469×10^3
1097.28	0.562	397	1677.06	2.1499×10^4	3.7337×10^3
1293.56	0.848	489	1677.06	2.1382×10^4	3.6842×10^3

Interpretation

Method consistency. The (ESTAR) value is closer to the ^{90}Y endpoint (∼2.28 MeV), while the Katz–Penfold inversion is higher. The offset is expected as ESTAR CSDA ranges include detailed stopping-power structure and density-effect corrections, whereas the Katz–Penfold power law is a single-exponent approximation. **Shielding implications.** The result illustrates that a *thin, low-Z layer* near a β source efficiently stops electrons with minimal bremsstrahlung. In a hybrid-reactor shield this logic generalises to a layered stack with low-Z liner for β/electron control, a hydrogenous section (water/PE) for fast-neutron slowing, a borated section for thermal capture, a high-Z (steel/lead) for γ attenuation, and heavy concrete for economical bulk shielding and skyshine control. Penetrations are treated with labyrinths/offsets and borated liners to suppress streaming. Ultimately, transport (MCNP/Serpent) sets thicknesses, while activation-foil checks and simple attenuation tests like this provide local validation during commissioning and maintenance.

VIII. CONCLUSIONS

Fusion–fission hybrids use strong, externally controllable sources to drive subcritical blankets for energy, breeding, and waste management. Materials and spectral tailoring near the first wall should prioritise multipliers over moderators when actinide fission and TBR are of most importance. Low-activation alloys like vanadium enable rapid dose reduction after shutdown, easing maintenance and waste handling. Activation foils tied to validated detector models form the backbone of hybrid diagnostics. Finally, robust and layered shielding that addresses both 14 MeV and fission-spectrum neutrons as well as capture gammas is essential for regulatory compliance and safe operations. Figures 1, 2, 4, 3 and Table I summarise the key measurements used here.

[1] R. Arnoux, "Velikhov sees hybrids as key to 'Nuclear Renaissance'," ITER Newsline (3 Dec 2012). Available at https://www.iter.org/node/20687/velikhov-sees-hybrids-key-nuclear-renaissance.

[2] D. Dalton, "China Aims To Operate World's First Hybrid Fusion–Fission Nuclear Plant By 2030," NucNet (28 Mar 2025). Available at https://www.nucnet.org/news/china-aims-to-operate-world-s-first-hybrid-fusion-fission-nuclear-plant-by-2030-3-5-2025.

[3] J. A. Maniscalco, D. H. Berwald, R. B. Campbell, R. W. Moir, and J. D. Lee, "Recent Progress in Fusion–Fission Hybrid Reactor Design Studies," *Fusion Science and Technology* **1**, 419–478 (1981). doi:10.13182/FST81-A19943.

[4] F. H. Tenney, "A Brief Review of the Fusion–Fission Hybrid Reactor," Princeton Plasma Physics Laboratory Report (1977). Available at https://www.osti.gov/servlets/purl/7329477.

[5] S. T. Perkins, E. F. Plechaty, and R. J. Howerton, "A Reevaluation of the ^{9}Be(n,2n) Reaction and Its Effect on Neutron Multiplication in Fusion Blanket Applications," *Nuclear Science and Engineering* **90**, 83–98 (1985). doi:10.13182/NSE85-A17433.

[6] F. A. Hernández-González and P. Pereslavtsev, "First principles review on the options for tritium breeder and neutron multiplier materials for breeding blankets in fusion reactors," EUROfusion preprint WPBB-PR(18)19890 (2018). Available at https://scipub.euro-fusion.org/wp-content/uploads/eurofusion/WPBBPR18_19890_submitted.pdf.

[7] C. W. Forsberg, "Fusion Blankets and Fluoride-Salt-Cooled High-Temperature Reactors," *Nuclear Technology* **206**, 1143–1170 (2020). doi:10.1080/00295450.2019.1691400.

[8] V. Philipps, "Tungsten as material for plasma-facing components in fusion devices," *Journal of Nuclear Materials* **415**, S2–S9 (2011). doi:10.1016/j.jnucmat.2011.01.110.

[9] Y. Ueda *et al.*, "Baseline high heat flux and plasma facing materials for fusion," *Nuclear Fusion* **57**, 092006 (2017). doi:10.1088/1741-4326/aa6b1d.

[10] T. Muroga *et al.*, "Vanadium alloys—overview and recent results," *Journal of Nuclear Materials* **307–311**, 547–554 (2002). doi:10.1016/S0022-3115(02)01253-9.

[11] D. L. Smith, "Reference vanadium alloy V–4Cr–4Ti for fusion application," *Journal of Nuclear Materials* **233–237**, 356–363 (1996). doi:10.1016/S0022-3115(96)00231-0.

[12] R. J. Kurtz and A. M. Yacout, "Present Status of Vanadium Alloys for Fusion Applications," PNNL report (2014). Available at https://www.pnnl.gov/publications/present-status-vanadium-alloys-fusion-appli

cations.

[13] National Nuclear Data Center (NNDC), "NuDat 3—V-52 decay radiation and level data," Brookhaven National Laboratory (accessed 3 Oct 2025). Available at https://www.nndc.bnl.gov/nudat3/ (navigate to nuclide 52V).

[14] Korea Atomic Energy Research Institute (KAERI) Nuclear Data, "V-52 basic data" (accessed 28 Sep 2025). Available at https://atom.kaeri.re.kr/cgi-bin/nuclide?nuc=V-52.

[15] ORTEC, *AN34 Experiments in Nuclear Science—Gamma-Ray Spectroscopy Using NaI(Tl)* (accessed 9 Oct 2025). Available at https://www.ortec-online.com/.

[16] ORTEC, *AN34 Experiments in Nuclear Science—Experiment 3* (mirror, accessed 1 Oct 2025). Available at https://www.ortec-online.com/resources.

[17] Images Scientific Instruments, "Geiger Counter Experiment #3: Detecting alpha, beta and gamma radiation" (accessed 30 Sep 2025). Available at https://www.imagesco.com/.

[18] G. F. Knoll, *Radiation Detection and Measurement*, 4th ed. (Wiley, Hoboken, 2010).

[19] W. R. Leo, *Techniques for Nuclear and Particle Physics Experiments* (Springer, 1994).

[20] H. Chan, "Neutron Activation Analysis Lab," California State University Northridge, course handout (accessed 10 Oct 2025). Available at https://www.csun.edu/.

[21] Mirion Technologies, "Technical Advantages of ISOCS/LabSOCS," Application Note C39530 (2019). Available at https://assets-mirion.mirion.com/prod-20220822/cms4_mirion/files/isocs-labsocs-app-note-c39530_LgZwJKK.pdf.

[22] Mirion Technologies, "LabSOCS™ Calibration Software" (accessed 6 Oct 2025). Available at https://www.mirion.com/products/technologies/spectroscopy-scientific-analysis/gamma-spectroscopy/gamma-spectroscopy-software/lab-applications/labsocs-calibration-software.

[23] A. Barba-Lobo *et al.*, "Robustness of LabSOCS calculating Ge detector efficiency," *Applied Radiation and Isotopes* **197**, 110854 (2023). doi:10.1016/j.apradiso.2022.110854.

[24] J. P. Stewart and D. Groff, "LabSOCS vs. source-based gamma-ray detector efficiency comparisons for nuclear power plant geometries," Mirion white paper (2002). Available at https://assets-mirion.mirion.com/prod-20220822/cms4_mirion/files/labsocs_PgYwXZp.pdf.

[25] L. Katz and A. S. Penfold, "Range–Energy Relations for Electrons and the Determination of Beta-Ray Endpoint Energies by Absorption," *Reviews of Scientific Instruments* **23**, 74–77 (1952). doi:10.1063/1.1746036.

[26] UK Government, *Managing Radioactive Substances and Nuclear Decommissioning: UK Policy Framework* (May 2024). Available at https://assets.publishing.service.gov.uk/media/6632371769098ded31fca7c1/managing-radioactive-substances-and-nuclear-decommissioning-uk-policy-framework.pdf.

[27] Korea Atomic Energy Research Institute (KAERI) Nuclear Data, "Au-198 basic data" (accessed 12 Oct 2025). Available at https://atom.kaeri.re.kr/cgi-bin/nuclide?nuc=Au198.

[28] Korea Atomic Energy Research Institute (KAERI) Nuclear Data, "In-116 including 116m (meta) state" (accessed 27 Sep 2025). Available at https://atom.kaeri.re.kr/cgi-bin/nuclide?nuc=In116.

[29] Z. Kis, B. Fazekas, J. Óstor, Zs. Révay, T. Belgya, G. L. Molnár, and L. Koltay, "Comparison of efficiency functions for Ge gamma-ray detectors in a wide energy range," *Nuclear Instruments and Methods in Physics Research Section A* **418**, 374–386 (1998). doi:10.1016/S0168-9002(98)00778-5.

[30] M.-C. Lépy, "Fitting in Gamma-Ray Spectrometry," ICRM/GSWG training course notes, LNHB/CEA (2015) (accessed 26 Sep 2025). Available at https://www.lnhb.fr/pdf/ICRM_GSWG/2018/Courses/M.C.Lepy_Fitting-applications.pdf.

[31] Japan Environmental Radioactivity Database (ENVRAD), *Gamma-ray Spectrometry using Germanium Semiconductor Detector* (2020) (accessed 5 Oct 2025). Available at https://www.envraddb.go.jp/en/wp-content/uploads/sites/3/2020/12/No.7_E.pdf.

[32] Nuclear-Power.com, "Neutron moderator—average logarithmic energy decrement" (accessed 8 Oct 2025). Available at https://www.nuclear-power.com/glossary/neutron-moderator-average-logarithmic-energy-decrement/.

[33] Mirion Technologies, "ProSpect™ Gamma-Ray Spectroscopy Software" (accessed 8 Oct 2025). Available at https://www.mirion.com/.

[34] NIST ESTAR (electrons): https://physics.nist.gov/PhysRefData/Star/Text/ESTAR.html.

Appendix A: Methods and Error Analysis (Aligned with Report Workflow)

(Dated: October 15, 2025)

1. A.1 Notation and propagation (single source of truth)

Spectra. CSV: {`Channel`, `Energy (keV)`, `Counts`}. Live times: sample $t_{\text{live}}^{(s)}$, background $t_{\text{live}}^{(b)}$.
CvT series. Arrays x (s), y (cps). For weighting only, a small stabiliser $\pi > 0$ avoids zero-variance bins.
Propagation (master rule). For any derived quantity $z = f(\boldsymbol{\theta})$ with parameter vector $\boldsymbol{\theta}$:

$$u^2(z) \;=\; \boldsymbol{g}^T \operatorname{cov}(\boldsymbol{\theta})\, \boldsymbol{g}, \qquad \boldsymbol{g} = \partial f / \partial \boldsymbol{\theta}. \tag{1}$$

All explicit formulas below are consistent with Eq. (1) and follow international guidance (GUM, NIST) and the PDG statistics review [7–12].

Variables and symbols (global).

C_s, C_b**:** gross counts in signal/background windows (dimensionless).

T, T_B**:** acquisition times for signal/background windows (s).

N**:** net counts after background subtraction (counts).

R**:** net rate $= N/T$ (cps).

A_c**:** activity at the start of counting (Bq).

$\boldsymbol{A_{\text{rem}}}$**: activity at removal time** (Bq).

$\varepsilon(E)$**:** full-energy-peak efficiency at energy E (dimensionless).

P_γ**:** absolute emission probability for a line (branching ratio).

λ**:** decay constant (s^{-1}); $T_{1/2} = \ln 2/\lambda$.

$u(\cdot)$**:** standard uncertainty; $u_r(\cdot) = u(\cdot)/(\cdot)$ relative.

2. A.2 Background subtraction (used everywhere)

Counts in a signal window with a separate background window:

$$N = C_s - \alpha C_b, \quad \alpha = \frac{T}{T_B}, \quad u^2(N) = C_s + \alpha^2 C_b, \tag{2}$$

with net rate $R = N/T$ and $u(R) = u(N)/T$. For spectra visualisation, use cps per bin: $\text{net}(E) = \frac{C^{(s)}(E)}{t_{\text{live}}^{(s)}} - \frac{C^{(b)}(E)}{t_{\text{live}}^{(b)}}$.

Variables and symbols (this subsection).

α**:** live-time scaling factor between background and signal (dimensionless).

$t_{\text{live}}^{(s)}, t_{\text{live}}^{(b)}$**:** dead-time–corrected live times for sample/background (s).

3. A.3 Carbon vs water moderation with ^{198}Au (411.8 keV)

Using the 411.802 keV line (NuDat3 [1]) and a sideband area (Eq. (2) or Eq. (7) below):

$$A_0 = \frac{N\,\lambda_{\text{Au}}}{\varepsilon(E_\gamma)\,P_\gamma\,[1 - e^{-\lambda_{\text{Au}} t_m}]}, \quad A_{\text{rem}} = A_0 e^{\lambda_{\text{Au}} \Delta t}. \tag{3}$$

Thermal flux per configuration $X \in \{\text{water}, \text{carbon}\}$:

$$\Phi_X = \frac{A_{\text{rem,X}}}{N_{\text{Au}}\,\sigma_{\text{eff}}\,[1 - e^{-\lambda_{\text{Au}} t_{\text{irr}}}]}. \tag{4}$$

Report the ratio (as in the main text)

$$R = \Phi_{\text{water}}/\Phi_{\text{carbon}}. \tag{5}$$

Uncertainty flow for R. Cancelling terms: because the same line, geometry, and analysis are used, $\varepsilon(E_\gamma)$, P_γ, N_{Au}, and σ_{eff} largely cancel in R.
Dominant terms: counting in N (both configurations) and small timing terms. Thus

$$\left(\frac{u(R)}{R}\right)^2 \approx \left[\frac{u(A_{\text{rem,water}})}{A_{\text{rem,water}}}\right]^2 + \left[\frac{u(A_{\text{rem,carbon}})}{A_{\text{rem,carbon}}}\right]^2. \tag{6}$$

Variables and symbols (this subsection).

λ_{Au}**:** decay constant for ^{198}Au (s^{-1}).

E_γ**:** γ-ray energy used (411.8 keV).

t_m**:** live (or real) counting time for the Au spectrum (s).

Δt**:** delay from removal to count start (s); used to back-correct to removal time.

N_{Au}**:** number of target nuclei in the foil (dimensionless).

σ_{eff}**:** effective (spectrum-averaged) activation cross section (cm^2).

t_{irr}**:** irradiation time (s).

Sideband option (if used).

$$N = C_s - \beta C_b, \quad \beta = \frac{w_{\text{sig}}}{w_{\text{sb}}}, \quad u^2(N) = C_s + \beta^2 C_b. \tag{7}$$

$w_{\text{sig}}, w_{\text{sb}}$**:** total energy widths of signal and sideband windows (keV).

β**:** sideband scaling factor (dimensionless).

4. A.4 Counting-vs-time (CvT) for ^{52}V half-life (Sec. ??)

Model and fit (non-linear least squares; SciPy [4]):

$$y(t) = B + Ae^{-kt}, \quad \sigma_i = \sqrt{y_i + \pi}. \quad \text{Fit } A, k \text{ to } y - \widehat{B}. \tag{8}$$

Half-life:

$$T_{1/2} = \frac{\ln 2}{k}, \quad u(T_{1/2}) = \frac{\ln 2}{k^2} u(k). \tag{9}$$

Diagnostics: quote χ^2/ν. If $\chi^2/\nu > 1$, inflate parameter errors by $\sqrt{\chi^2/\nu}$ (PDG prescription [12]).
Variables and symbols (this subsection).

$y(t)$**:** net count rate versus time (cps).

B**:** time-independent background level (cps).

A**:** amplitude at $t = 0$ above background (cps).

k**:** decay constant fitted from CvT (s^{-1}).

π**:** small positive stabiliser added inside σ_i for numerical robustness (cps).

$\widehat{B}$**:** estimated background from an early time window (cps).

5. A.5 HPGe efficiency from Eu-152 (used for indium) and residual scatter

Eu decay to measurement time:

$$A_{\text{meas}} = A_{\text{ref}}\, e^{-\lambda_{\text{Eu}}(t_{\text{meas}}-t_{\text{ref}})}, \quad \lambda_{\text{Eu}} = \frac{\ln 2}{T_{1/2}^{(\text{Eu})}}. \tag{10}$$

Per-line efficiency point:

$$\varepsilon_i = \frac{N_i}{A_{\text{meas}} T_i P_{\gamma,i}}, \quad \left(\tfrac{u(\varepsilon_i)}{\varepsilon_i}\right)^2 = \left(\tfrac{u(N_i)}{N_i}\right)^2 + \left(\tfrac{u(P_{\gamma,i})}{P_{\gamma,i)}}\right)^2 + \left(\tfrac{u(A_{\text{meas}})}{A_{\text{meas}}}\right)^2. \tag{11}$$

Fit model (as in the report):

$$\log_{10}\varepsilon = a_0 + a_1 \log_{10} E + a_2 (\log_{10} E)^2. \tag{12}$$

Residual term (exactly as used): add an *extra* relative scatter of $\boxed{16.506\%}$ in quadrature to account for fit residuals:

$$u_r^2\big(\varepsilon_{\text{fit}}\big) \;\leftarrow\; u_r^2\big(\varepsilon_{\text{fit}}\big) + (0.16506)^2. \tag{13}$$

Scale terms for later indium use (as in report): adopt $u_r(A_{\text{Eu}}) = 5\%$ and $u_r(P_\gamma\ (\text{In})) = 2\%$.

Variables and symbols (this subsection).

A_{ref}**:** Eu source activity at reference date (Bq).

A_{meas}**:** Eu activity at measurement (Bq).

$t_{\text{ref}}, t_{\text{meas}}$**:** reference and measurement times (d or s).

$T_{1/2}^{(\text{Eu})}$**:** Eu-152 half-life (y).

N_i**:** net counts in Eu line i (counts).

T_i**:** live time for Eu line i (s).

$P_{\gamma,i}$**:** absolute emission probability for Eu line i (dimensionless).

a_0, a_1, a_2**:** regression coefficients of the log–quadratic model.

6. A.6 In-116m per-line activities and *inverse-variance* average

Activity at count start from line i:

$$A_{c,i} = \frac{N_i}{T\,\varepsilon(E_i)\,P_{\gamma,i}}, \qquad A_{\text{rem},i} = A_{c,i}\, e^{\lambda \Delta t}. \tag{14}$$

Per-line uncertainty (matches report budget).

$$\left(\frac{u(A_{\text{rem},i})}{A_{\text{rem},i}}\right)^2 = \underbrace{\left(\frac{u(N_i)}{N_i}\right)^2}_{\text{counting}} + \underbrace{(0.05)^2}_{A_{\text{Eu}}\ \text{scale}} + \underbrace{(0.02)^2}_{P_\gamma\ (\text{In})} + \underbrace{(0.16506)^2}_{\varepsilon\ \text{fit scatter}} + (\text{small timing/live-time terms if applicable}). \tag{15}$$

Inverse-variance weighted mean. Let σ_i be the (statistical) standard uncertainty of $A_{\text{rem},i}$ *excluding* the common-mode scale terms (Eu 5%, P_γ 2%, and 16.506% scatter). Then

$$\overline{A}_{\text{rem}} = \frac{\sum_i A_{\text{rem},i}/\sigma_i^2}{\sum_i 1/\sigma_i^2}, \qquad u_{\text{stat}}^2(\overline{A}_{\text{rem}}) = \frac{1}{\sum_i 1/\sigma_i^2}. \tag{16}$$

Finally, attach the common-mode relative terms to the *combined* mean:

$$u_{\text{tot}}^2(\overline{A}_{\text{rem}}) = u_{\text{stat}}^2(\overline{A}_{\text{rem}}) + \Big[(0.05)^2 + (0.02)^2 + (0.16506)^2\Big]\ \overline{A}_{\text{rem}}^{\,2}. \tag{17}$$

Goodness-of-fit for the lines:

$$\chi^2 = \sum_i \frac{(A_{\text{rem},i} - \overline{A}_{\text{rem}})^2}{\sigma_i^2}, \quad \nu = n - 1;\ \text{inflate } u_{\text{stat}} \text{ by } \sqrt{\chi^2/\nu} \text{ if } \chi^2/\nu > 1. \tag{18}$$

Variables and symbols (this subsection).

T**:** live time of the indium count (s).

E_i**:** indium line energy for peak i (keV).

Δt**:** removal-to-count delay (s).

σ_i**:** statistical standard uncertainty of $A_{\mathrm{rem},i}$ used for weighting (Bq).

$\overline{A}_{\mathrm{rem}}$**:** inverse-variance combined activity at removal (Bq).

7. A.7 Thermal neutron flux from indium (as used in report)

With irradiation time t_{irr} and removal-to-count delay Δt:

$$\Phi = \frac{\overline{A}_{\mathrm{rem}}}{N_{\mathrm{In}}\,\sigma_{\mathrm{eff}}}\;\frac{1}{1-e^{-\lambda t_{\mathrm{irr}}}}. \tag{19}$$

Uncertainty. Common-mode terms carried from Sec. A.6 remain common in Φ. Writing $G = (1-e^{-\lambda t_{\mathrm{irr}}})^{-1}$,

$$\left(\frac{u(\Phi)}{\Phi}\right)^2 = \left(\frac{u(\overline{A}_{\mathrm{rem}})}{\overline{A}_{\mathrm{rem}}}\right)^2 + u_r^2(N_{\mathrm{In}}) + u_r^2(\sigma_{\mathrm{eff}}) + \left[\frac{\lambda e^{-\lambda t_{\mathrm{irr}}}}{1-e^{-\lambda t_{\mathrm{irr}}}}\,u(t_{\mathrm{irr}})\right]^2 + \text{ (small timing } \Delta t \text{ if included).} \tag{20}$$

Variables and symbols (this subsection).

N_{In}**:** number of target ^{115}In nuclei in the foil (dimensionless).

σ_{eff}**:** effective activation cross section for the flux spectrum (cm^2).

t_{irr}**:** irradiation time (s); $G = (1-e^{-\lambda t_{\mathrm{irr}}})^{-1}$ is the build-up factor.

8. A.8 Peak localisation and sidebands

Locate: around a marker E_k (from NuDat3 [1]) search $[E_k-\Delta, E_k+\Delta]$ for the maximum net bin; refine with a 3-point parabola

$$E^\star = -\frac{b}{2a} \text{ from } y \approx aE^2+bE+c, \quad \Delta E = E^\star - E_k. \tag{21}$$

Area: adjacent sidebands with equal total width to the signal window give Eq. (7); include live-time scaling via Eq. (2) when using a separate background spectrum.

Variables and symbols (this subsection).

E_k**:** tabulated marker energy (keV); Δ is the search half-width (keV).

a, b, c**:** local quadratic coefficients used for centroid refinement.

$E^\star$**:** refined centroid estimate (keV); $\Delta E = E^\star - E_k$.

9. A.9 Aluminium β attenuation (shielding section)

Areal density for thickness t_{mm}:

$$\mathcal{R} = \rho(0.1)t_{\mathrm{mm}}\ [\mathrm{g\,cm^{-2}}], \quad u(\mathcal{R}) = \rho(0.1)u(t_{\mathrm{mm}}). \tag{22}$$

Net rate $r_{\mathrm{net}} = r_g - r_b$ with Poisson errors; fit the initial exponential region:

$$\ln r_{\mathrm{net}} = mt_{\mathrm{mm}} + c, \quad d_{1/2} = \frac{\ln 2}{|m|}, \quad u(d_{1/2}) = \frac{\ln 2}{m^2}u(m). \tag{23}$$

Map practical range to $E_{\max}$ using Katz–Penfold [6] or NIST ESTAR [5].

Uncertainty mapping to $E_{\max}$. Include interpolation/fit-model term u_{model}:

$$u^2(E_{\max}) \approx \left(\frac{\partial E}{\partial \mathcal{R}}\, u(\mathcal{R})\right)^2 + u^2_{\text{model}}. \tag{24}$$

Variables and symbols (this subsection).

t_{mm}**:** total Al thickness (mm); ρ is Al density ($2.70\,\text{g}\,\text{cm}^{-3}$).

$\mathcal{R}$**:** areal density ($\text{g}\,\text{cm}^{-2}$); defined to avoid confusion with flux ratio R.

r_g, r_b**:** gross and background rates (cps); $r_{\text{net}} = r_g - r_b$.

m, c**:** slope/intercept from the semilog fit; $d_{1/2}$ is the half-thickness (mm).

$E_{\max}$**:** inferred endpoint energy (MeV); u_{model} covers ESTAR/KP model/interp. error.

References

[1] National Nuclear Data Center, *NuDat 3*, Brookhaven National Laboratory, https://www.nndc.bnl.gov/nudat3/ (accessed current study).

[2] G. F. Knoll, *Radiation Detection and Measurement*, 4th ed., Wiley (2010).

[3] Mirion Technologies, *LabSOCS/ISOCS Efficiency Calibration*, application notes and user manuals, https://www.mirion.com/.

[4] P. Virtanen *et al.*, "SciPy 1.0: Fundamental Algorithms for Scientific Computing in Python," *Nat. Methods* **17**, 261–272 (2020).

[5] NIST, *ESTAR: Stopping Power and Range Tables for Electrons*, https://physics.nist.gov/PhysRefData/Star/Text/ESTAR.html.

[6] L. Katz and A. Penfold, "Range-Energy Relations for Electrons and the Determination of Beta-Ray Endpoint Energies by Absorption," *Rev. Mod. Phys.* **24**, 28–44 (1952).

[7] JCGM 100:2008, *Evaluation of measurement data — Guide to the expression of uncertainty in measurement (GUM)*, Joint Committee for Guides in Metrology (BIPM), available at https://www.bipm.org/documents/20126/2071204/JCGM_100_2008_E.pdf.

[8] JCGM GUM-1:2023, *Guide to the expression of uncertainty in measurement — Part 1: Introduction to the GUM and related documents*, JCGM (BIPM), https://www.bipm.org/documents/20126/194484570/JCGM_GUM-1/.

[9] JCGM GUM-6:2020, *Guide to the expression of uncertainty in measurement — Part 6: Developing and using measurement models*, JCGM (BIPM), https://www.bipm.org/documents/20126/2071204/JCGM_GUM_6_2020.pdf.

[10] B. N. Taylor and C. E. Kuyatt, *Guidelines for Evaluating and Expressing the Uncertainty of NIST Measurement Results*, NIST Technical Note 1297 (1994), https://nvlpubs.nist.gov/nistpubs/legacy/tn/nbstechnicalnote1297.pdf summary at https://www.nist.gov/pml/nist-technical-note-1297.

[11] A. Possolo and B. Toman, *Simple Guide for Evaluating and Expressing the Uncertainty of NIST Measurement Results*, NIST Technical Note 1900 (2015), https://nvlpubs.nist.gov/nistpubs/TechnicalNotes/NIST.TN.1900.pdf.

[12] G. Cowan (for the Particle Data Group), *Statistics*, in *Review of Particle Physics* (2024), https://pdg.lbl.gov/2024/reviews/rpp2024-rev-statistics.pdf.

Appendix B: Detector Fundamentals for the Instruments Used

Theory, manufacturer notes, operating conditions, and uncertainties

Geiger–Müller (G–M) counter with thin mica window

Theory. A Geiger–Müller tube consists of a central anode wire within a gas-filled cathode cylinder. At the operating bias in the Geiger region, a single primary ion pair triggers a Townsend avalanche that flows along the wire, producing a standardised pulse, whose height is independent of the particle's initial energy. Quench gas terminates the discharge, preventing continuous conduction and afterpulses. Because pulse height is not energy-proportional, a G-M counter measures presence and relative intensity only, not spectra. After each avalanche the tube is insensitive for a dead time τ_d and at high rates this leads to undercounting, described approximately by the model $m = n/(1 + n\tau_d)$ or, when avalanches extend dead time, by the model $m = n\, e^{-n\tau_d}$.

A schematic of a bench G–M counter is shown in Fig. 1.

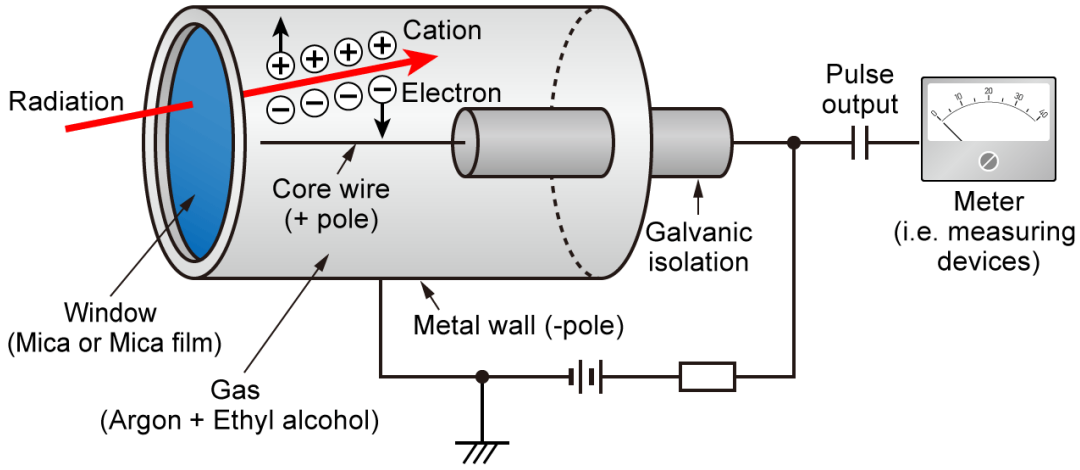

Figure 1: Geiger–Müller tube with thin mica window, central anode wire, quench gas, and readout chain. Pulses correspond to saturated avalanches and are counted by a scaler. (One open-source schematic example: Wikimedia Commons file "Geiger-Muller-counter-en.png" by Svjo-2.)[11]

Use in this work. The G-M counter was used to demonstrate β attenuation in aluminium (Sec. A.7).

Manufacturer note. The teaching set employs a thin mica end-window tube in a compact, mains-powered scaler supplied with the lab kit (tube type comparable to the LND "pancake" class). The window holds good sensitivity to low-energy β and to α at very close geometry, while the steel body acts as an absorber for low-energy photons.

Operating conditions and uncertainties. Statistical uncertainty follows Poisson counting, so $u(R) = \sqrt{C}/t$ for a net count C in live time t. Systematic effects are dominated by geometry set-up (source distance and alignment), window self-absorption for low-energy β, and gain drift if the power supply is not allowed to stabilise and these were controlled through a warm-up period of at least 15 min, and repetition of readings. References: Knoll [1], Leo [2].

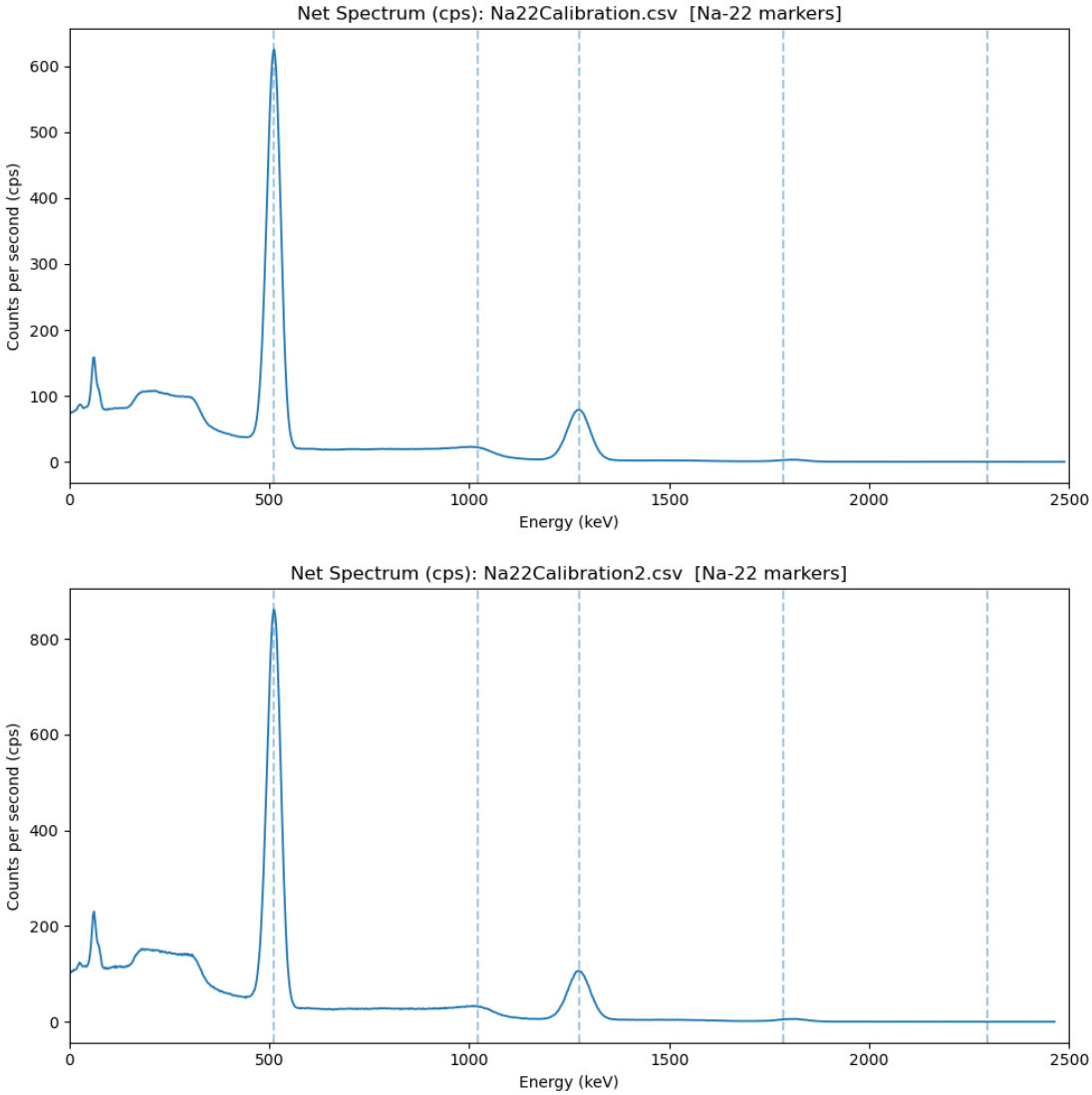

Figure 2: NaI(Tl) two-point energy calibration with a ^{22}Na source: top, initial calibration; bottom, repeat confirming stable gain and resolution over the session. The 511 keV and 1274.5 keV photopeaks are visible in both spectra.

3×3 ORTEC NaI(Tl) scintillation detector with PMT

Theory. In NaI(Tl) scintillators, energy deposited by γ rays produces scintillation photons via activator levels, with a dominant decay constant of a few hundred nanoseconds. A bialkali photomultiplier tube converts the optical signal into an electrical pulse; the pulse height is approximately proportional to deposited energy. The energy resolution is governed primarily by photoelectron statistics and non-proportional light yield, with an approximate relation $(\Delta E/E)_{\mathrm{FWHM}} \approx 2.35/\sqrt{N_{\mathrm{pe}}}$. Spectra exhibit a Compton continuum, a sharp Compton edge, and full-energy peaks where all energy is absorbed; escape features are uncommon in NaI(Tl).

A typical NaI(Tl)+PMT source-detector-shield configuration is sketched in Fig. 3.

Use in this work. The NaI(Tl) system provided rapid spectra for background characterisation, for moderation comparisons using ^{198}Au foils at 411.8 keV, and for decay monitoring where line separation was not limiting (see Fig. 2 in the main text). A two-point energy calibration was performed with ^{22}Na using the 511 keV and 1274.5 keV lines in the same geometry as the activation foils. Background spectra were acquired with lead shielding and the same

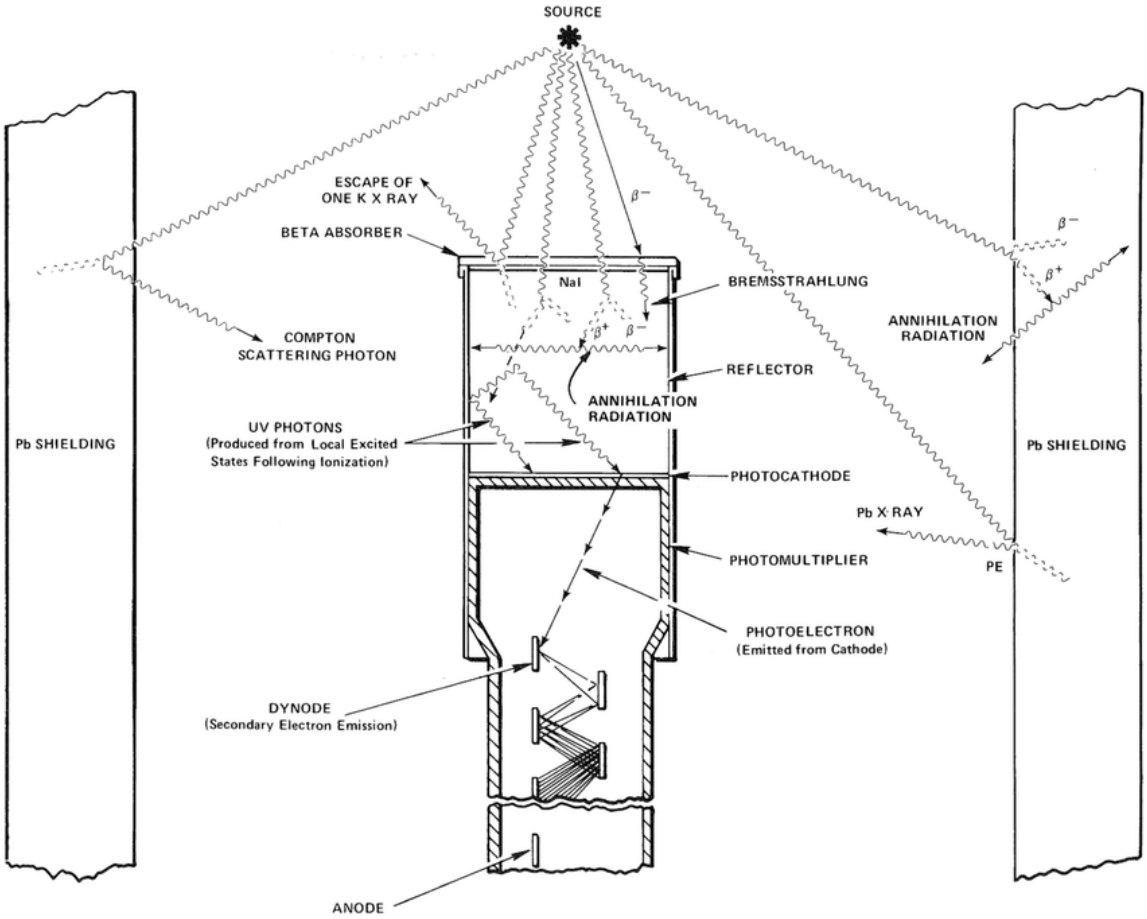

Figure 3: Scintillation detector with photomultiplier readout. The schematic highlights dominant γ interactions in NaI(Tl), scintillation and photoelectron production, and dynode multiplication. [9, 10]

shaping and threshold settings as the sample runs. Net peak areas were obtained by Gaussian fits with linear sidebands. A representative two-point ^{22}Na calibration is shown in Fig. 2.

Manufacturer note. The scintillator/PMT assembly was supplied by ORTEC as a sealed 3×3 crystal coupled to a head-on PMT through an optical window, read out by standard spectroscopy electronics. A Hamamatsu PMT handbook [4] provides the underpinning PMT performance assumptions (quantum efficiency, gain, afterpulsing).

Operating conditions and uncertainties. Typical performance in this configuration is $\Delta E/E \sim 7$–8% at 662 keV, with broader peaks at lower energies due to non-proportionality. Counting statistics in the region of interest dominate peak-area uncertainty for short live times; background subtraction adds in quadrature via $u^2(N) = C_\mathrm{s} + C_\mathrm{b}$, scaled by live-time ratios where appropriate. Energy-scale uncertainty is mainly from short-term gain drift but this was mitigated by a 15 min warm-up and periodic checks on the 1461 keV marker. For quantitative comparisons across moderators, geometry and acquisition settings were held constant so that efficiency and emission-probability systematics cancel in ratios. Residual systematics include self-attenuation in the moderator blocks and small source-to-detector distance variations; these were addressed by fixed measurements and repeated measurements. References: Knoll [1], Leo [2], Gilmore [3], Hamamatsu [4].

Mirion/Canberra coaxial HPGe detector with Eu-based efficiency (LabSOCS cross-check)

Theory. High-purity germanium detectors are reverse-biased, fully depleted diodes. Gamma interactions create electron–hole pairs at $\approx 2.96\,\mathrm{eV}$ per pair at 77 K. Because fluctuations are sub-Poissonian (Fano factor $F \sim 0.1$), intrinsic resolution is excellent and the observed FWHM combines Fano statistics with electronic noise and charge-collection terms, $\Delta E^2_{\mathrm{FWHM}} \simeq (2.35)^2 F\varepsilon E + \Delta E^2_{\mathrm{el}} + \Delta E^2_{\mathrm{cc}}$. Coaxial HPGe delivers keV-scale peak widths across the MeV range, enabling unambiguous line identification and robust quantification.

A diode cross-section indicating p^+ and n^+ contacts, depletion and neutral regions, and aluminium electrodes is shown in Fig. 4. Comparable schematics and explanations appear in NRC training material and Mirion's HPGe lab notes.[12, 13]

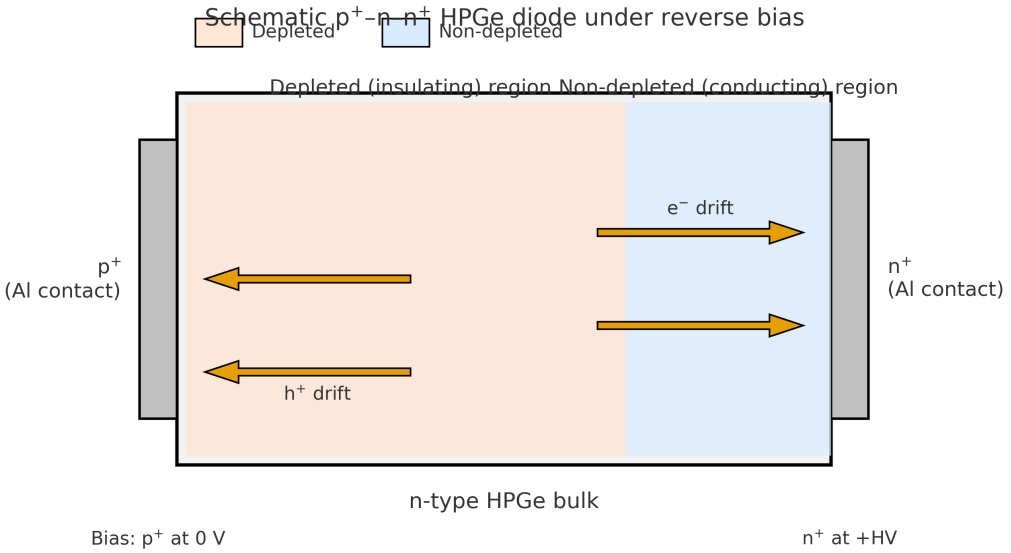

Figure 4: Schematic p^+–n–n^+ HPGe diode with aluminium contacts under bias, indicating depleted (insulating) and non-depleted (conducting) regions; arrows denote carrier drift. This schematic is consistent with standard descriptions for coaxial HPGe contacts and depletion behaviour (see, e.g., NRC training notes and Mirion's HPGe laboratory experiment).[12, 13, 14]

Use in this work. The HPGe system was used for absolute activity determination of $^{116\mathrm{m}}$In. *For the indium analysis, the full-energy-peak efficiency $\varepsilon(E)$ was obtained empirically* from a certified multi-γ europium source counted in the *identical* geometry as the samples. The source certificate activity A_{ref} was decayed to the counting date using the stated half-life, and per-line efficiencies were computed as

$$\varepsilon(E_i) = \frac{N_{\mathrm{net},i}}{t_\ell \, A_{\mathrm{Eu}}(t) \, I_{\gamma,i}},$$

then fitted with a simple log–quadratic in $\log_{10} E$ and applied to the indium peaks. A LabSOCS model of the same detector and scene was generated as an *independent cross-check*; its predicted $\varepsilon(E)$ was compared to the Eu-based calibration for consistency.

Manufacturer note. The detector is a Mirion (formerly Canberra) coaxial HPGe coupled to standard spectroscopy electronics and an MCA. A LabSOCS/ISOCS characterisation exists for the instrument and geometry and was used only for an independent comparison of predicted vs. measured efficiencies.

Operating conditions and uncertainties. The detector was operated on liquid-nitrogen. Energy calibration employed at least two well-separated lines; residuals of $\lesssim 0.3\,\mathrm{keV}$ were taken

as acceptable. For activity from a peak at E,

$$A_c = \frac{N_{\mathrm{net}}}{t_\ell \, \varepsilon(E) \, I_\gamma},$$

with N_{net} the background-subtracted area, t_ℓ the dead-time–corrected live time, $\varepsilon(E)$ the *Eu-derived* absolute efficiency, and I_γ the emission probability. Statistical uncertainty follows Poisson propagation through A_c. Systematic components propagated for the indium results were limited to those entering the Eu calibration (certificate activity and half-life of Eu, branching ratios I_γ, and the regression dispersion of the Eu fit) plus geometry tolerances; *LabSOCS model uncertainties were not propagated into the indium activities*, as LabSOCS served only as a separate consistency check. References: Knoll [1], Gilmore [3], ISO 11929 [6], PDG statistics review [7], Mirion application notes.

General counting, dead time, and detection limits

Theory and practice. For net counts C acquired in live time t, the rate $R = C/t$ has standard uncertainty $u(R) = \sqrt{C}/t$; when a separate background B is subtracted, variances add as $u^2(C_{\mathrm{net}}) = C_{\mathrm{s}} + C_{\mathrm{b}}$ (scaled by live-time ratios for differing presets). Spectroscopy systems report instrument dead time; when large, a correction $n = m/(1 - m\tau_d)$ is adequate for most modern MCAs, but high-rate early-time points in decay curves should be scrutinised for pile-up. References: Currie [5], ISO 11929 [6], PDG [7], ORTEC notes [8].

References

[1] G. F. Knoll, *Radiation Detection and Measurement*, 4th ed., Wiley (2010).

[2] W. R. Leo, *Techniques for Nuclear and Particle Physics Experiments*, Springer (1994).

[3] G. Gilmore, *Practical Gamma-ray Spectrometry*, 2nd ed., Wiley (2008).

[4] Hamamatsu, *Photomultiplier Tubes: Basics and Applications*, 3rd ed. (2007), https://www.hamamatsu.com/.

[5] L. A. Currie, "Limits for qualitative detection and quantitative determination," *Analytical Chemistry* **40**, 586–593 (1968).

[6] ISO 11929 series, *Determination of the characteristic limits for measurements of ionising radiation*, ISO (2019–2022).

[7] Particle Data Group, "Statistics" review, in *Review of Particle Physics* (2024).

[8] ORTEC, Application notes on dead time, pile-up, and throughput in nuclear spectroscopy (various), https://www.ortec-online.com/.

[9] ORTEC, *AN34 Experiments in Nuclear Science (Fourth ed.): 3. Gamma-Ray Spectroscopy Using NaI(Tl)* (accessed current study), https://www.ortec-online.com/-/media/ametekortec/fourth-edition-experiments/fourth-ed-3.pdf.

[10] ORTEC, *AN34 Experiments in Nuclear Science (Third ed.): 3. Gamma-Ray Spectroscopy Using NaI(Tl)* (accessed current study), https://www.ortec-online.com/-/media/ametekortec/third%20edition%20experiments/3-gamma-ray-spectroscopy-using-nai-tl.pdf.

[11] Wikimedia Commons, "File:Geiger-Muller-counter-en.png" (open-licence schematic), https://commons.wikimedia.org/wiki/File:Geiger-Muller-counter-en.png.

[12] U.S. NRC, *Semiconductor Detectors* (training document, Jan 2010), ML11229A683, https://www.nrc.gov/docs/ML1122/ML11229A683.pdf.

[13] Mirion, "High-Resolution Gamma-Ray Spectroscopy with HPGe Detectors: Lab Experiments" (education article), https://www.mirion.com/discover/knowledge-hub/articles/education/high-resolution-gamma-ray-spectroscopy-with-hpge-detectors-lab-experiments.

[14] University of Liverpool, PHYS389 lecture notes, "Germanium detectors – Planar and Coaxial" (slides), https://hep.ph.liv.ac.uk/~gcasse/Phys389/PHYS389-lecture13.pdf.

Appendix C:
Data, Calibration, and Reproducibility

Marcus Turner-Wood
Department of Physics, University of Liverpool
sgmturn2@liverpool.ac.uk

October 15, 2025

C.1 Conventions & Directory Layout

- **Data root:** `Data/` (CSV UTF-8; decimal point; header row where applicable).
- **Spectra CSVs:** `Channel, Energy (keV), Counts`. For count–vs–time series, the "Energy (keV)" column stores **time (s)**.
- **Timestamps:** ISO 8601 (local). Live/real times recorded in CSV metadata lines where present.
- **Geometry units:** mm (distances), $\mathrm{g\,cm^{-3}}$ (densities).
- **Recommended naming:** `Experiment_Sample_Run_YYYY-MM-DD.csv`.

C.2 Dataset Index (by experiment)

Filename (relative to `Data/`)	Instrument/Exp.	Description
`3/CarbonModerated.csv`	NaI(Tl), Au-198 (Moderator)	Carbon moderator spectrum; 411.8 keV ROI.
`3/WaterModerated.csv`	NaI(Tl), Au-198 (Moderator)	Water moderator spectrum; same geometry.
`3/b/Indium.csv`	HPGe, In-116m	High-resolution HPGe spectrum.
`3/b/Eu_peaks.csv`	HPGe, Eu-152 (cal)	Eu lines used for efficiency validation.
`4/V-52EnergySpectra.csv`	NaI(Tl), V-52 (Vanadium)	Energy spectrum; line ID near 1490 keV.
`4/V52 2.csv`	NaI(Tl), V-52 (Vanadium)	Count–vs–time series (1 s dwell).
`5/foil_reference.csv`	GM / Sr-90 (metadata)	Foil material, thickness, area; for range calc.
`5/measurements.csv`	GM / Sr-90 (run log)	Thickness steps, live/background, geometry.
`Background\&Calibrations/Background&Calibration.csv`	NaI(Tl) (background)	NaI background used in calibration.

continued on next page

Filename	Instrument/Exp.	Description
Background\&Calibrations/BackgroundGermanium.csv	HPGe (background)	HPGe background, calibration geometry.
Background\&Calibrations/Na22Calibration.csv	NaI(Tl) (calibration)	Na-22 calibration spectrum (primary).
Background\&Calibrations/Na22Calibration2.csv	NaI(Tl) (calibration)	Na-22 calibration spectrum (repeat).

C.3 Dataset Cards & Quick Previews

Dataset: 3/WaterModerated.csv **Category:** Au-198 (Moderator)
Instrument: NaI(Tl)
Notes: Water moderator; 411.8 keV line for flux ratio.

```
Start Time, Tue Sep 23 14:24:16 GMT+0100 2025
Energy calibration,  Offset: -28.945449829101563, Slope: 2.4586737155914307, Quadratic: 0
Live Time (s), 436.67
Real Time (s), 436.74
Elapsed Computational, 0
Spectrum
Channel, Energy (keV), Counts
1, -26.486776113510132, 0
2, -24.0281023979187, 0
3, -21.56942868232727, 4
4, -19.11075496673584, 33
5, -16.65208125114441, 27
6, -14.193407535552979, 23
7, -11.734733819961548, 14
8, -9.276060104370117, 25
9, -6.8173863887786865, 24
10, -4.358712673187256, 28
11, -1.9000389575958252, 9
12, 0.5586347579956055, 23
13, 3.017308473587036, 26
14, 5.475982189178467, 30
15, 7.9346559047698975, 21
16, 10.393329620361328, 30
17, 12.852003335952759, 30
18, 15.31067705154419, 30
19, 17.76935076713562, 34
20, 20.22802448272705, 36
21, 22.68669819831848, 50
22, 25.145371913909912, 35
23, 27.604045629501343, 40
24, 30.062719345092773, 37
25, 32.521393060684204, 31
26, 34.980066776275635, 31
27, 37.438740491867065, 38
28, 39.897414207458496, 47
```

Dataset: 3/CarbonModerated.csv **Category:** Au-198 (Moderator)
Instrument: NaI(Tl)
Notes: Carbon moderator; ratio $R = \phi_{\text{th}}^{(water)} / \phi_{\text{th}}^{(carbon)}$.

```
Start Time, Tue Sep 23 16:29:35 GMT+0100 2025
Energy calibration,  Offset: -28.945449829101563, Slope: 2.4586737155914307, Quadratic: 0
Live Time (s), 381.66
```

```
Real Time (s), 381.81
Elapsed Computational, 0
Spectrum
Channel, Energy (keV), Counts
1, -26.486776113510132, 0
2, -24.0281023979187, 0
3, -21.56942868232727, 2
4, -19.11075496673584, 53
5, -16.65208125114441, 62
6, -14.193407535552979, 79
7, -11.734733819961548, 67
8, -9.276060104370117, 69
9, -6.8173863887786865, 73
10, -4.358712673187256, 74
11, -1.9000389575958252, 68
12, 0.5586347579956055, 84
13, 3.017308473587036, 85
14, 5.475982189178467, 66
15, 7.9346559047698975, 59
16, 10.393329620361328, 89
17, 12.852003335952759, 83
18, 15.31067705154419, 100
19, 17.76935076713562, 111
20, 20.22802448272705, 92
21, 22.68669819831848, 109
22, 25.145371913909912, 109
23, 27.604045629501343, 100
24, 30.062719345092773, 104
25, 32.521393060684204, 79
26, 34.980066776275635, 85
27, 37.438740491867065, 90
28, 39.897414207458496, 106
```

Dataset: 4/V-52EnergySpectra.csv **Category:** V-52 (Energy spectrum)
Instrument: NaI(Tl)
Notes: Peak near 1490 keV; Compton continuum noted.

```
Start Time, Mon Jan 1 00:00:00 GMT+0000 1900
Energy calibration,  Offset: -28.69147300720215, Slope: 2.433980941772461, Quadratic: 0
Live Time (s), 570.205914
Real Time (s), 570.558879
Elapsed Computational, 0
Spectrum
Channel, Energy (keV), Counts
1, -26.257492065429688, 0
2, -23.823511123657227, 0
3, -21.389530181884766, 3
4, -18.955549240112305, 53
5, -16.521568298339844, 112
6, -14.087587356567383, 93
7, -11.653606414794922, 94
8, -9.219625473022461, 95
9, -6.78564453125, 94
10, -4.351663589477539, 110
11, -1.9176826477050781, 106
12, 0.5162982940673828, 92
13, 2.9502792358398438, 110
14, 5.384260177612305, 119
15, 7.818241119384766, 118
16, 10.252222061157227, 134
17, 12.686203002929688, 124
18, 15.120183944702148, 138
19, 17.55416488647461, 123
20, 19.98814582824707, 137
```

```
21, 22.42212677001953, 118
22, 24.856107711791992, 153
23, 27.290088653564453, 150
```

Dataset: `4/V52 2.csv` **Category:** V-52 (Count vs time)
Instrument: NaI(Tl)
Notes: 1 s dwell; fit $y(t) = B + Ae^{-kt}$; record fit window and dead time.

`2.csv`

Dataset: `3/b/Indium.csv` **Category:** In-116m (Spectrum)
Instrument: HPGe
Notes: Main lines: 416.9, 818.7, 1097.3, 1293.6 keV.

```
Start Time, Tue Sep 30 12:26:03 GMT+0100 2025
Energy calibration,  Offset: -0.13534560799598694, Slope: 0.24128232896327972, Quadratic: 0
Live Time (s), 1677.06
Real Time (s), 1683.06
Elapsed Computational, 0
Spectrum
Channel, Energy (keV), Counts
1, 0.10593672096729279, 3
2, 0.3472190499305725, 13
3, 0.5885013788938522, 2108
4, 0.829783707857132, 3993
5, 1.0710660368204117, 163
6, 1.3123483657836914, 64
7, 1.5536306947469711, 24
8, 1.7949130237102509, 44
9, 2.0361953526735306, 39
10, 2.2774776816368103, 59
11, 2.51876001060009, 90
12, 2.7600423395633698, 79
13, 3.0013246685266495, 109
14, 3.242606997489929, 102
15, 3.483889326453209, 101
16, 3.7251716554164886, 75
17, 3.9664539843797684, 77
18, 4.207736313343048, 77
19, 4.449018642306328, 59
20, 4.6903009712696075, 71
21, 4.931583300232887, 46
22, 5.172865629196167, 38
23, 5.414147958159447, 45
```

Dataset: `3/b/Eu_peaks.csv` **Category:** Eu-152 (Lines)
Instrument: HPGe
Notes: Eu peaks used to validate efficiency curve.

```
Start Time, Wed Oct 8 10:41:01 GMT+0100 2025
Energy calibration,  Offset: -0.15331940352916718, Slope: 0.24095268547534943, Quadratic: 0
Live Time (s), 506.32
Real Time (s), 507.07
Elapsed Computational, 0
Spectrum
Channel, Energy (keV), Counts
1, 0.08763328194618225, 0
2, 0.3285859674215317, 0
```

```
3, 0.5695386528968811, 50
4, 0.8104913383722305, 76
5, 1.05144402384758, 31
6, 1.2923967093229294, 25
7, 1.5333493947982788, 24
8, 1.7743020802736282, 17
9, 2.0152547657489777, 58
10, 2.256207451224327, 36
11, 2.4971601366996765, 46
12, 2.738112822175026, 36
13, 2.9790655076503754, 41
14, 3.220018193125725, 38
15, 3.460970878601074, 34
16, 3.7019235640764236, 34
17, 3.942876249551773, 43
18, 4.1838289350271225, 46
```

Dataset: `Background\&Calibrations/BackgroundCalibration.csv` **Category:** NaI(Tl) background
Instrument: NaI(Tl)
Notes: Background spectrum used during NaI calibration.

File not found at `Data/Background\&Calibrations/BackgroundCalibration.csv`. Place the CSV there to show a preview.

Dataset: `Background\&Calibrations/BackgroundGermanium.csv` **Category:** HPGe background
Instrument: HPGe
Notes: HPGe background in calibration geometry.

File not found at `Data/Background\&Calibrations/BackgroundGermanium.csv`. Place the CSV there to show a preview.

Dataset: `Background\&Calibrations/Na22Calibration.csv` **Category:** NaI(Tl) calibration
Instrument: NaI(Tl)
Notes: Na-22 calibration spectrum (primary).

File not found at `Data/Background\&Calibrations/Na22Calibration.csv`. Place the CSV there to show a preview.

Dataset: `Background\&Calibrations/Na22Calibration2.csv` **Category:** NaI(Tl) calibration
Instrument: NaI(Tl)
Notes: Na-22 calibration spectrum (repeat).

File not found at `Data/Background\&Calibrations/Na22Calibration2.csv`. Place the CSV there to show a preview.

Dataset: `5/measurements.csv` **Category:** Sr-90 run log
Instrument: GM
Notes: Thickness steps, live times, background runs, geometry, HV.

```
measurement_id,foils,gross_counts,live_time_s
1,,258,1
2,1,100,1
,,,
4,7,162,10
,,,
,,,
,,,
,,,
9,"7,5",114,10
10,"5,6",24,10
11,"11,1",221,10
12,"7,1",158,10
13,"2,3,4,8,6",84,60
14,"6,11",20,10
15,"6,2",18,10
16,"6,5,1",25,10
,,,
18,7,165,10
,,,
20,"7,1,5",72,10
21,"9,11",194,10
22,"10,11",93,10
23,"9,10",184,10
24,"6,1",26,10
```

Dataset: `5/foil_reference.csv` **Category:** Sr-90 foil reference
Instrument: GM
Notes: Foil material, mass, thickness, area; used to compute areal density.

```
foil_id,thickness_mm,sigma_thickness_mm,note
1,0.28,0.01,
2,2.46,0.01,
3,2.46,0.01,
4,2.46,0.01,
5,0.27,0.01,
6,3.41,0.01,
7,1.54,0.01,
8,4.41,0.01,
9,0.96,0.01,
10,1.2,0.01,
11,1.17,0.01,
```

C.4 Calibration & Energy Scale

C.4.1 NaI(Tl) energy calibration with ^{22}Na

The two dominant photopeaks (511 and 1274.5 keV) from `Background\&Calibrations/Na22Calibration.csv` (and the repeat run) define a linear scale $E \approx a + b\,\text{Channel}$. If peak locations are already extracted, record them here:

Expected (keV)	Channel	Measured (keV)	Residual (keV)	Peak counts
511.00	220	511.963	+0.963	376,586
1274.50	530	1274.152	-0.348	47,688

Fitted **linear calibration** (example values):

$$E\ [\text{keV}] \;=\; a + b\,\text{Channel}, \qquad a = -28.9454\ \text{keV}, \quad b = 2.45867\ \text{keV/ch}$$

C.4.2 Background spectra used during calibration

Backgrounds used with the calibration geometry are included above for reproducibility.

C.5 LabSOCS Geometry & Materials (summary)

Detector model/serial _____ / _____
Characterisation file _____ (LabSOCS ver. _____)
Sample container/matrix _____ (density _____ $\mathrm{g\,cm^{-3}}$)
Source–detector distance _____ mm (tolerance ±_____ mm)
Endcap/window _____ (dead layer _____ µm)
Pb shielding _____ mm (grade _____)

C.6 Sr-90 Attenuation Setup (from metadata)

Files: `5/foil_reference.csv` and `5/measurements.csv`.
The Sr-90 β attenuation analysis uses:

- **Foil parameters** (material, density, thickness, area) from `5/foil_reference.csv`.
- **Run ladder** (thickness steps, live/background times, geometry) from `5/measurements.csv`.

Derived quantities (to be computed in analysis):

$$\ln r = m\,\mathcal{R} + c, \qquad d_{1/2} = \frac{\ln 2}{|m|}, \quad R_\beta \simeq 10\,d_{1/2}, \quad \mathcal{R} = \rho\, t,$$

with ρ from the foil reference and t from the thickness ladder in the run log.

To record after fitting: $m =$ _____ $\mathrm{mm^{-1}}$ (or convert to $(\mathrm{g\,cm^{-2}})^{-1}$ via $\mathcal{R}$), $d_{1/2} =$ _____ mm, $R_\beta =$ _____ mm, $\chi^2/\nu =$ _____.

C.7 Processing Provenance

- Scripts / notebooks: `analysis.ipynb`, `process_indium.py` (commit: _____)
- Software: Prospect _____, LabSOCS _____, Python _____, NumPy/SciPy _____
- Geometry files: _____
- Random seeds (if any): _____

C.8 QA/QC Checks

- NaI background stability: K-40 at 1461 keV drift < _____ keV during session
- V-52 CvT: early dead-time fraction < _____% (trim earliest bins if higher)
- Geometry repeatability: ±_____ mm; Eu/Indium matched geometry
- Au-198: confirm 675.9 and 1087.7 keV peaks consistent with 411.8 keV
- Sr-90: confirm semilog linear window selection; report χ^2/ν and residuals